HHS Public Access

Author manuscript

Biomaterials. Author manuscript; available in PMC 2020 March 01.

Published in final edited form as:

Biomaterials. 2019 March ; 195: 111–123. doi:10.1016/j.biomaterials.2018.12.031.

Meningeal inflammatory response and fibrous tissue remodeling around intracortical implants: an *in vivo* two-photon imaging study

JR Eles[a,b], **AL Vazquez**[a,b,c], **TDY Kozai**[a,b,d,e,f], and **XT Cui**[a,b,d]

[a]Bioengineering, University of Pittsburgh, United States

[b]Center for the Neural Basis of Cognition, University of Pittsburgh and Carnegie Mellon University, United States

[c]Radiology, University of Pittsburgh, United States

[d]McGowan Institute for Regenerative Medicine, University of Pittsburgh, United States

[e]NeuroTech Center of the University of Pittsburgh Brain Institute, United States

[f]Center for Neuroscience, University of Pittsburgh, United States

Abstract

Meningeal inflammation and encapsulation of neural electrode arrays is a leading cause of device failure, yet little is known about how it develops over time or what triggers it. This present work characterizes dynamic changes of meningeal inflammatory cells and collagen-I in order to understand the meningeal tissue response to neural electrode implantation. We use *in vivo* two-photon microscopy of CX3CR1-GFP mice over the first month after electrode implantation to quantify changes in inflammatory cell behavior as well as meningeal collagen-I remodeling. We define a migratory window during the first day after electrode implantation hallmarked by robust inflammatory cell migration along electrodes in the meninges as well as cell trafficking through meningeal venules. This migratory window attenuates by 2 days post-implant, but over the next month, the meningeal collagen-I remodels to conform to the surface of the electrode and thickens. This work shows that there are distinct time courses for initial meningeal inflammatory cell infiltration and meningeal collagen-I remodeling. This may indicate a therapeutic window early after implantation for modulation and mitigation of meningeal inflammation.

Keywords

intravital imaging; neural interface; foreign body response; hydrogel; meninges; brain-computer interface

Corresponding author, 5057 Biomedical Science Tower 3, 3501 Fifth Avenue, Pittsburgh, PA, USA. xic11@pitt.edu; Fax: +1-412-648-9076; Tel: +1-412-383-6672.

1. Introduction

Penetrating neural electrodes are essential tools for electrophysiological monitoring and electrical stimulation of neurons to enable brain-computer interfaces, neuromodulation, and longitudinal neuroscience research [1–8]. Despite their clinical promise, neural electrodes have limited long-term performance due to their poor integration into host tissue. [9–16]. As a consequence, electrode recording failure within months to years after implantation has been reported in rodent [17, 18], cat[19], and primate models [20, 21] for chronically implanted electrode devices.

Many strategies have been pursued to improve the longevity of neural electrodes, with most focused on alleviating glial scarring and neurodegeneration within the brain parenchyma [22]. The neural tissue response, however, is not the only biological source of failure. The fibrous meningeal tissue at the surface of the brain can proliferate and encapsulate aspects of the electrode array that reside at the surface of the brain (commonly referred to as the “platform” or “base” of an electrode array). The meninges consists of layers of fibrous tissue at the brain’s surface (figure 1(a)) that provide mechanical protection to the brain [23], harbor the major arteriole and venule inputs and outputs of the brain [24], and is essential in controlling brain inflammation and waste clearance [25–28]. After injury, however, inflammatory cell influx and increased collagen synthesis can create thickening of the meningeal tissues [28–30].

In the context of neural implants, implantation of large arrays in non-human primates and in the clinical setting requires a large (>16 cm^2) craniotomy that can significantly affect bone regrowth and wound healing [21, 31, 32]. These large “critical-sized” defects can still impair bone repair even when the bone is replaced after surgery [32]. As a result of critical-sized cranial defects, collagen within the craniotomy tends to thicken and bone regrowth is limited, but this can be improved by filling the craniotomy with scaffolds [33–35]. This may explain findings that meningeal tissue and collagen-I progressively grows around and under the electrode device and can lead to ejection of the device from the cortex [19]. In their landmark studies analyzing failure modes of 78 Utah style electrode arrays implanted in non-human primates, Barrese et al. show that 53% of chronic device failures occur due to meningeal encapsulation and ejection of devices, with more arrays displaying some degree of meningeal encapsulation [21, 36]. Similar or greater rates of this phenomena have been observed for Utah array implants in rodent [37, 38] and cat [19] models. Meningeal encapsulation mirrors the foreign body response to implanted devices in other non-CNS tissues, which ultimately results in fibrous encapsulation of the device [39, 40]. Interestingly, meningeal encapsulation of neural devices is prevalent for chronically implanted sub- and epi-dural electrocorticographic electrode grids as well [41–44]. This suggests that the encapsulation response does not require traumatic brain penetration to proceed.

Nonetheless, several studies have also reported cellular exchange between the meningeal and intracortical compartments adjacent to penetrating electrode arrays. Suspected fibroblast migration from the meninges along the electrode shank can occur in implants that protrude through the meninges, but not in implants that are fully embedded in the cortex [45–48]. A similar cell migration route may be partly responsible for the large population of blood-

borne macrophage at the intracortical tissue-electrode interface. Previous studies have shown that over 60% of monocytes at the interface come from outside instead of migration of resident brain microglia [12].

The current, limited solutions for preventing meningeal encapsulation of device extend to creating physical barriers between the device and meningeal tissue [49, 50] and pharmacologically inhibiting fibroblast proliferation [51], but these solutions have not changed the narrative on meningeal encapsulation [21, 52]. To create targeted prevention and mitigation strategies for meningeal encapsulation, we must understand the triggers and control switches for the fibrous growth. In the present work, we use *in vivo* two-photon microscopy in a mouse model for implanted intracranial electrodes to quantify meningeal inflammatory cell response and meningeal collagen-I remodeling over the first month post-implantation. We build on our previous results showing rapid dynamic cell behavior at the meningeal surface [52] to define a migratory window for meningeal inflammatory cells. Over the first day after implant, meningeal inflammatory cells show rapid migration along the surface of the electrode at the meningeal-electrode interface and through pial vessels. Over the next weeks, there is low cell migration in these compartments and stable, but variable, inflammatory cell density in the tissue surrounding the electrode. By the first month post-implant, meningeal collagen remodels to conform to the surface of the electrode and thickens. These findings ultimately suggest that there is a rapid meningeal response in the early period after implantation that may present a therapeutic window to alter the long-term outlook for meningeal encapsulation of neural electrodes arrays.

2. Materials and Methods

2.1. Animals and surgery

This study used a total of 8 mice, with a total of 12 craniotomies. Of these, 6 craniotomies were filled with silicone elastomer, 5 craniotomies were filled with saline, and 1 craniotomy was filled with a hydrogel sealant. One subject had significant bubble formation within the silicone at the meningeal-electrode interface and was only used for meningeal thickness quantification. One additional subject failed to recover from implantation by day 2 of implantation and was removed from the study. All subjects were CX3CR1-GFP transgenic mice with GFP expression in brain microglia and macrophage as well as circulating leukocytes such as myeloid cells, NK cells, dendritic cells, and neutrophils controlled by the CX3CR1 promotor (Jackson Laboratories, Bar Harbor, ME)[53]. All animals were male and between 3–6 months of age at time of implantation. Implantation was based on previous surgical optimization[52]. Briefly, animals were anesthetized with 75mg/kg ketamine and 10mg/kg xylazine and head-fixed with ear bars. Animals' temperature and respiration was maintained with a heating pad and oxygen line. After cleaning with isopropyl alcohol and betadine, the animals' scalps were resected and bilateral craniotomies (~4×3mm) over visual, motor, and somatosensory cortices were drilled with a high-speed dental drill. Non-functional, 3mm single shank silicon planar electrode arrays (NeuroNexus, Ann Arbor, Michigan) were manually implanted in the center of the craniotomy targeting somatosensory cortex (figure 1(a), *left*). Dura was not removed prior to implantation. Implants were inserted to approximately 1mm, which was assessed by inserting until all electrode sites were

submerged in tissue and confirmed by post-mortem analysis of explanted electrodes (figure 6(d)). Implants were approximately inserted 30° angle, which was gauged by protractor confirmed by post-insertion imaging. For all implants, angle of insertion was on average 34.8° with a standard deviation of 10.3°. The tab of the electrode was broken off with surgical microscissors after implantation such that the broken end was level with the top of the skull (figure 1(a), *right*). Any electrode fragments in the imaging window were removed by gentle saline washes. Minimal movement of the electrode was noted while cutting the shank. This was confirmed by the minimal dural defect observed after implantation (figure 5(a)) and lack of bleeding after cutting the electrode. Craniotomies were either filled with a sealant material or with pH controlled, osmotically balanced saline that was sterilized by manufacturer prior to use. The sealant material was either an *in situ* forming silicone elastomer sealant (Kwik-Sil, World Precision Instruments, Sarasota, FL), or a novel *in situ* forming hydrogel sealant (described below). All sealant materials were applied through sterilized applicator tips or needles. After filling the craniotomy, it was covered with a cover glass. The cranial window was secured with light-curable cement (Composite Flowable; Henry Schein, NY, USA), and animals were allowed to recover. Animals showed no signs of infection throughout the study. All procedures and experimental protocols were approved by the University of Pittsburgh, Division of Laboratory Animal Resources and Institutional Animal Care and Use Committee in accordance with the standards for humane animal care as set by the Animal Welfare Act and the National Institutes of Health Guide for the Care and Use of Laboratory Animals.

2.2. Hydrogel preparation and validation

For one animal, the craniotomy was sealed with <10μL of an *in situ* forming hydrogel (referred to as PEG/PEI hydrogel). The gel was prepared by mixing 10% w/v 4-arm poly(ethylene) glycol (10 kDa, JenKem Technology USA, Plano, TX, USA) with 10% v/v branched polyethylenimine (25 kDa, Sigma-Aldrich) in a 10:1 ratio in sterile saline, which is similar in composition to commercially available, FDA approved PEG/PEI hydrogels [54]. Hydrogel precursor solutions were filter sterilized prior to mixing. All gels cured within 30s. The biocompatibility of the hydrogel was determined by a conditioned media study on a Highly Aggressive Proliferating Immortalized (HAPI) microglial cell line (provided by Dr. Xiaoping Hu, University of Pittsburgh) as previously described [55–57]. HAPI cells were selected as they are of a leukocyte lineage, and therefore similar to the CX3CR1(+) cells we observe in the *in vivo* portion of this study. HAPI cells were plated in at 10^5 cells/well in a 24-well plate. Cells were grown in control media (DMEM/F12 with 10% Fetal Bovine Serum and 1% penicillin-streptomycin, ThermoFisher Scientific) until 80% confluency. Media was replaced with either fresh control media, or control media that had been conditioned with a freshly crosslinked PEG/PEI hydrogel overnight. Conditioning did not affect pH, which was measured by pH strips. After 1 day of exposure, cells were stained with a Live/Dead Cell Viability Assay (ThermoFisher Scientific) and imaged with a fluorescence microscope. Cell viability was determined by comparing the area of each image occupied with live cells to the area of each image occupied with dead cells (analysis completed on the NIH software ImageJ).

2.3. In vivo *two-photon Imaging*

At 0.5, 0.75, 1, 2, 4, 7, 14, 21, and 28 days post implant (dpi), animals were sedated with 1–1.5% isoflurane and head-fixed with ear bars for imaging. For vascular contrast, animals received intraperitoneal injections of sulforhodamine 101 (SR101) (~0.05 cc; 1 mg/ml). Animals were placed under a two-photon laser scanning microscope with a Bruker scan head (Prairie Technologies, Madison, WI), TI:sapphire laser tuned to 920 nm (Mai Tai DS; Spectra-Physics, Menlo Park, CA), light collection through non-descanned photomultiplier tubes (Hamamatsu Photonics KK, Hamamatsu, Shizuoka, Japan), and a 16x, 0.8 numerical aperture water immersion objective (Nikon Inc., Milville, NY) as previously described [52, 58, 59]. Laser power was maintained between 20–40 mW. All images were collected through Prairie View software. For each imaging session, "Z-stack" tissue volumes from each craniotomy (410 × 410 × 82μm XYZ at a resolution of 0.8 X 0.8 X 2 μm) were scanned at 1 minute intervals (frame scan rate: 0.69Hz; line scan rate: 357 Hz) for 15–30 minutes. Additional Z-stacks were collected with filters to resolve second harmonic generation (SHG) at half the laser wavelength (~460nm), which enables intrinsic imaging of collagen-I (shown in blue in figure 1(b), *top left*). For a subset of animals (3 from the silicone sealant group and 2 from the saline sealant group), devices were explanted at the experimental endpoint and imaged under two-photon microscopy. Additional devices were damaged during explantation and not viable for explant analysis.

2.4. Non-human primate explant analysis

To compare and contrast these murine findings with higher order animals, we examined the *ex vivo* meningeal collagen around a 10×10 shank Utah style array (Blackrock Microsystems, Salt Lake City, UT) that had been implanted in the motor cortex of a rhesus macaque for ~2.5 years (tissue was donated by the Motorlab, directed by Dr. Andrew Schwartz, at University of Pittsburgh). Following transcardial perfusion with 4% paraformaldehyde, the brain was removed with the Utah array and surrounding bone left intact. After post-fixation in 10% paraformaldehyde, micro computed tomography (microCT) was performed with a multi-modal Siemens Inveon micro-CT/SPECT/PET system (Inveon, Siemens Inc., Knoxville, TN, USA) as previously described[37]. The Utah array and surrounding tissue (>5mm margin) was dissected out of the brain. Brain tissue adjacent to one side of the Utah array was sectioned away with a Vibratome until the shanks of one edge of the device were visible. These shanks were imaged for second harmonic generation imaging as described in section 2.3.

2.5. Image processing, analysis, and statistics

2.5.1. Cell velocity analysis—CX3CR1(+) cellular element migration along the electrode's surface at the meningeal-electrode interface was estimated by a "cell migration index" . First, time-series z-stacks of the silicone sealant group were preprocessed by a median filter (3×3 pixel kernel). For each time frame, images along the Z-axis were summed to project the 3D Z-stack into a single 2D plane. Motion between frames was corrected by a recursive rigid body transformation (StackReg plugin for ImageJ software[60]). A region of interest (ROI) around the meningeal-electrode interface was manually-defined based on the boundary between the electrode's surface and the SHG signal of the meningeal collagen-I. A

custom Matlab script (MathWorks, Boston, MA) was used to determine the “cell migration index” for the CX3CR1(+) cellular elements in each time-series. First, to determine which pixels were part of CX3CR1(+) cellular elements, images were binarized based on an image intensity threshold (mean pixel intensity + the standard deviation of pixel intensities for each frame). The difference in number of CX3CR1(+) cellular elements within the ROI between consecutive frames was used to estimate the amount of migration during each frame. This number was normalized to the total number of CX3CR1(+) cellular elements to produce the cell migration index, where a “0” value indicates no migration and a “1” value indicates that all CX3CR1(+) cellular elements showed movement. The cell migration index was averaged across frames for each time-point to enable statistical comparisons across time-points. All animals with silicone filled sealants were used for this analysis (n = 5), however, due to animal attrition and large motion artifacts in some imaging sessions, n = 4 from 0.5–1dpi and 14–21dpi, n = 5 from 2–7dpi, and n =3 at 28dpi. Statistical comparisons over time were performed with one-way ANOVA and Tukey HSD post-tests (Matlab; significance: $p < 0.05$).

Individual cell velocities were also calculated by manual tracking at 0.5–1dpi in ImageJ. Velocities are presented as mean velocity over 5–30min windows. Cell diameters were based on the major axis of ellipses fitted to each migrating cell. Migratory direction preference was calculated by defining movement “toward interface” as negative X-direction movement and “away from the interface” as positive X-direction movement, where the X-direction is along the length of the electrode. Preference was defined by net movement/ absolute value of total movement for each cell, where a “−1” value would indicate that a cell moved exclusively toward the interface, a “+1” value would indicate that a cell moved exclusively away from the interface, and a value of “0” would indicate that the cell moved equal distance toward and away from the interface.

2.5.2. Cell density analysis—Density of meningeal CX3CR1(+) cellular elements within 100μm of the implanted electrode was determined for silicone sealed craniotomies over time. A custom Matlab script was used to automatically segment meningeal cells from cortical cells based on the SHG collagen-I signal. A maximum intensity projection of the SHG z-stack was used to find the Z-location with the most intensity collagen-I signal for each XY coordinates. This information was used to fit a cubic polynomial surface over the surface of the brain using the “fit” function in Matlab’s Curve Fitting Toolbox. Each fit was manually inspected. To determine meningeal density, the number of pixels with CX3CR1(+) cellular elements (defined by a threshold set to the mean pixel intensity plus the standard deviation of image intensity of the maximum intensity Z-projection image) within ± 10μm of the fitted meningeal surface were summed. The sample region was confined to within 100μm of the implanted electrode as defined by the distance transform (“bwdist” function in Matlab). All animals with silicone filled sealants were used for this analysis (n = 5), however, due to animal attrition and large motion artifacts in some imaging sessions, n = 4 from 0.5–1dpi and 14–21dpi, n = 5 from 2–7dpi, and n =3 at 28dpi. The total area of the meningeal CX3CR1(+) signal was normalized to the total area of sampled meningeal surface. Statistical analysis of changes in density over time was carried out with a one-way ANOVA (Matlab).

2.5.3. Blood vessel trafficking analysis—To determine the extent of leukocyte trafficking through large pial vessels in silicone sealed or saline filled craniotomies, vessels labeled with SR101 were first identified as either venule or arteriole by measuring vessel dilation over 0.5 to 2dpi, where venules showed >10μm dilation as previously described [61]. A total of 7 venules and 5 arterioles over 6 animals were identified (). To track the amount of cellular trafficking, images were preprocessed with a median filter (3×3 pixel kernel). The maximum intensity projection of Z-stack slices that contained the center of the pial vessels along the XY plane was taken and motion was corrected by recursive rigid body transformation (StackReg plugin for ImageJ). For image series with low SR101 leakage, vessel ROIs could be segmented by creating a binary mask of vessels in the SR101 channel 3D Z-stacks to exclude all non-vessel pixels (example images shown in figure 4(a), *right*). Following definition of the vessel ROIs, the CX3CR1 channel was binarized using the IsoData threshold technique[62], and the number of CX3CR1(+) cells were counted for each frame using ImageJ Particle Analysis particles (particles <10μm^2 in area were discounted as noise). The average number of CX3CR1(+) cells over each imaging session was quantified. This analysis does not capture if cells cross the vessel wall or not. The number of trafficking cells in and the diameter venules and arterioles at 0.5–1dpi and 2–4dpi were compared by two-way ANOVA with Tukey's HSD post-hoc tests (Matlab; significance: $p < 0.05$).

2.5.4. Meningeal shape and thickness analysis—To assess if the meninges remodeled around the electrode after implantation, the margin of collagen-I tissue at the meninges-electrode interface was traced with the "getline" function in Matlab. Given the parabola-shaped nature of the collagen margin, we fit a 2nd degree polynomial to our trace using the "polyfit" function in Matlab and calculated curvature at the model's vertex. In this assessment, larger curvature means that the collagen-I margin is more separated from the electrode's surface, while less curvature implies that the collagen-I margin is flatter and more conformal against the face of the electrode. Changes in curvature over time were assessed by one-way ANOVA with Tukey's HSD post-hoc tests (Matlab; significance: $p < 0.05$). Curvature measurements within 12–24h were averaged together for the 1dpi value for each animal. For this analysis, all silicone sealed animals that survived for at least 21 dpi were used, resulting in n = 4 for 1–21dpi and n = 3 for 28dpi. A custom Matlab script was also used to automate the measurement of meningeal thickness in 3D Z-stacks with SHG images for both the silicone and saline sealed craniotomies. Following a 3D median filter (5×5×5 pixel kernel), a maximum intensity projection along the Z-axis was taken of the SHG signal. The 2D projection was used to manually defined an ROI drawn around the SHG(+) collagen-I signal surrounding the implants. The 3D z-stacks were then binarized based on a threshold of 0.5*mean pixel intensity of the maximum intensity projection ROI. Holes were filled in the binarized 3D stack with the "imfill" function in Matlab. Binarized images were manually inspected to ensure that a mask of the SHG(+) collagen-I was extracted. The thickness of the meninges was determined by taking the sum of pixels along the Z-axis at each XY location in the ROI. Sums were multiplied by Z-axis resolution (2μm). Any XY location in which the SHG(+) signal exceeded the depth of the Z-stack was automatically removed. To compare the thickness at 1dpi and the experimental endpoint (21–28dpi, depending on the animal) for the silicone and saline sealant groups, two-way ANOVA analysis with Tukey's HSD post-hoc tests were used (Matlab; significance: p <

0.05). Thickness measurements within 12–24h were averaged together for the 1dpi value for each animal. All animals with visible SHG signal within 100 μm of the electrode were used for this analysis: n = 6 for the silicone group at 1dpi, n= 5 for all other groups.

3. Results

Fibrous meningeal encapsulation and ejection of chronically implanted electrode arrays is one of the most common causes for electrode recording failure. To understand the progression of meningeal inflammation that can lead to fibrous encapsulation, we implanted 7 CX3CR1-GFP mice with single shank Michigan-style silicon electrode devices and used two-photon microscopy to quantify changes in inflammatory leukocyte behavior and meningeal collagen from 12h to 28 days post implant (dpi).

3.1. A migratory window for rapid CX3CR1(+) cell movement along electrode shank in the meningeal compartment

By 0.5 dpi, we noted robust migration on the implanted electrode device's surface that largely subsided by the end of the first week post implant (supplementary movie 1; figure 2(a)). Between 7–28dpi, cells on the probe appeared to aggregate and spread along the surface of the device, and had unclear boundaries between cells. Due to the ambiguous boundaries of individual cells, quantification of cell movement from 0.5–28dpi relied on counting the changes in number of CX3CR1(+) pixels (determined by a threshold) during each imaging session. Electrodes implanted in craniotomies that were filled with saline became buried in tissue by 7–14dpi, and were not included in cell migration quantification (see section 3.5.). Consistent with our qualitative assessment, there was significantly greater cell migration along the surface of the device at 0.5 – 1dpi compared to 4–28dpi (figure 2(b); one-way ANOVA $p < 0.00001$; Tukey HSD post-hoc tests $p < 0.05$ for all 0.5–1dpi to 4–28dpi comparisons except for 0.5dpi compared to 7 dpi). The shapes of 30 migrating cells from 0.5–1dpi were measured by ellipse fitting and each cell's position was tracked for at least 5 minutes to determine cell velocity (figure 2(c)). Due the tight clumping of cells at time points after 1dpi, it was not feasible to track cell velocities on the electrode's surface. Nonetheless, our migration index results (figure 2(a)) suggest that there is little migration during this period. From 0.5–1 dpi, cells had a mean diameter of 10.31 ± 3.46 μm velocity of 3.04 ± 2.31 μm/min (mean ± SEM), with no apparent correlation between these two parameters (linear regression $r^2 = 0.02$). These speeds are >60-fold greater than microglial cell body migration toward electrode implants at the same time points [61]. Migration direction preference was determined by normalizing the net distance traveled along the length of implant (where "-" is toward the interface and "+" is away from the interface as noted in figure 2(a)) to the absolute value of the total distance traveled along the length of the implant (figure 2(d)). Individual cells show preference for going toward the interface, away from the interface, or neither, but without a discernable average preference (−0.14 ± 0.70, mean ± std. dev.), suggesting that cells are potentially responding to a multitude of chemotactic and other environmental cues.

3.2. Variable meningeal CX3CR1(+) cell densities around the implant over the first month

In addition to inflammatory cell migration along the device, another critical metric to understanding meningeal-electrode interactions is inflammatory cell density changes in the meningeal tissue surrounding the implant. To cleanly differentiate meningeal inflammatory cells from brain inflammatory cells, we defined the meningeal surface by meningeal collagen-I through second harmonic generation imaging (figure 3(a)). Cellular density in ROIs along this boundary were quantified over time for silicone filled craniotomies in four animals (figure 3(b)). Saline filled craniotomies were not quantified over time because electrodes became fully buried in brain tissue underneath the meninges by 7–14dpi (see section 3.5.), impeding our ability to define the electrode's location There was some fluctuation in cell density within 100μm of the implant between animals and over time, but no statistically significant change in cell density (one-way ANOVA $p = 0.5961$). The variability over time may echoes the high variability of the cortical response to implanted electrodes [63].

3.3. Robust CX3CR1(+) cell trafficking through venules at ≤1dpi decreases by 2–4dpi

To understand potential sources of the inflammatory cells that migrate along the surface of the device and fluctuate in the surrounding meningeal tissue, we quantified CX3CR1(+) cellular trafficking through blood vessels. Venules could be differentiated from arterioles based on a dilatory response over the first days after implantation (figure 4(a) *left*, 4(b)) as previously described [61]. Venules dilation began to subside by 4dpi (5.0 ± 2.58 μm reduction in diameter, $p < 0.01$), which is consistent with other reports [64]. ROIs confined to within vasculature could be defined (figure 4(a), *right*) and the number of CX3CR1(+) cells in these ROIs over each imaging session could be quantified by automated particle analysis. This analysis does not capture if cells cross the vessel wall or not. Over the first 4 days, we quantified 692 trafficking cells with a mean diameter of 9.56 ± 4.57 μm (mean ± std. dev.). We noted that most detected cell trafficking was confined to venules within the first day after implantation (figure 4(c)). Due to our relatively slow image acquisition rate (frame rate: 0.69Hz), it is likely that we only captured trafficking of leukocytes that were adhered to the surface of blood vessels [65]. In this case, the lack of leukocyte adhesion to arterioles is consistent with previous findings [66, 67]. To confirm these observations, we statistically compared the number of trafficking cells in venules and arterioles at the 0.5–1dpi period and 2–4dpi period (figure 4(c)). There were significant effects between vessel types (two-way ANOVA: $p < 0.001$), with Tukey's post-hoc tests confirming that there were significantly more leukocytes trafficked through venules at 0.5–1dpi compared to all other groups.

3.4. Collagen-I at the meningeal-electrode interface remodels over the first month post-implant

While CX3CR1(+) cell migration along implanted electrodes and through venules peaks within the first day after implantation, collagen-I remodeling occurred over a period of weeks (figure 5(a)). After implantation, collagen-I was torn at the insertion site, resulting in a parabola-shaped defect in the meninges. By two weeks post-implant, however, the collagen had begun to remodel and was flatter and more conformal to the face of the electrode. We

quantified this by fitting a parabola to the collagen-I margin at the meningeal-electrode interface and calculating the curvature at the parabola's vertex (figure (5(b)). The curvature of the margin changed over the first month (one-way ANOVA, $p < 0.001$), with significantly reduced curvature between 14–28 dpi compared to 1–4dpi (Tukey's HSD Post-Hoc test, $p < 0.05$). This reduction confirms that the collagen did remodel over the first month and became more conformal to the flat surface of the electrode. In addition to changes in the shape of the meningeal-electrode interface, the meningeal tissue in the craniotomy thickened over the first month. Meningeal thickness could be quantified through automated measurements upper and lower bounds of the collagen-I(+) meningeal tissue along the Z-axis (figure 5(c)). Within 1dpi, meningeal thickness was consistent between animals, regardless of the craniotomy being filled with silicone or saline (silicone: 21.61 ± 7.84 μm; saline: 18.36 ± 1.20 μm; mean ± SEM). By the endpoint (21–28dpi), the meninges had thickened for each animal (silicone: 43.06 ± 8.17 μm; saline: 40.20 ± 7.84 μm; mean ± SEM). There was a statistically significant effect for changes in thickness over time, but not between sealant material (two-way ANOVA: $p < 0.0005$). While all animals showed thickening between 1 dpi and endpoint, there was high variability in the amount of thickening. As a result, post-hoc tests revealed trending significant differences between 1dpi and endpoint for the silicone ($p = 0.076$) and saline ($p = 0.057$).. As a note, the implants in saline filled craniotomies were buried in meningeal tissue by 7–14dpi, and so their locations could not always be identified. Meningeal thickness measurements for these animals were based on estimates of their last known location based on vascular landmarks and implant location.

3.5. Implants in saline-filled craniotomies become buried in meningeal tissue by 14dpi

In animals with silicone-sealed craniotomies, electrodes were fixed in place by silicone had an edge that remained outside of the meninges. In animals with saline-filled craniotomies and without the silicone sealant to fix the implant in place, electrodes were progressively buried in the meningeal tissue (figure 6(a)). For each time-point, we determined if the meningeal-facing end of the implanted device was fully buried in CX3CR1(+) cells or not ($n = 5$; figure 6(b)). By 7–14dpi, all implants were found submerged in meningeal tissue. For some animals, we could still locate the implant after it was fully buried in tissue and confirmed that the electrode was indeed under remodeled meningeal collagen-I (figure 6(c)). After sacrifice, we explanted devices (2 from saline filled craniotomies and 3 from silicone filled craniotomies) and qualitatively examined them with two-photon microscopy (figure 6(d)). While it is unclear how many adherent cells were removed during the explantation process, we noted that the remaining cells had distinct morphologies between the saline and silicone craniotomies. Namely, CX3CR1(+) cells adhered to devices in silicone-filled craniotomies were larger and more densely distributed along the device than cells adhered to devices in saline-filled craniotomies. The latter devices were completely buried in tissue by 7–14dpi, and so may not have been subjected to micromotion-related strain or diffusive exchange with the meninges [46] [45].

3.6. Additional considerations for hydrogel sealants: cell migration through gel matrix

Throughout this study, we noted that there was no cellular or dye infiltration into silicone sealants. In order to explore if meningeal cell infiltration was possible in porous, hydrophilic

hydrogels, we filled one craniotomy with an *in situ* forming hydrogel composed of poly(ethylene) glycol and polyethyleneimine (PEG/PEI gel) that is a non-resorbable variant to FDA approved PEG/PEI gels [68]. The gel showed no significant cytotoxicity issues *in vitro* (supplementary figure 1). *In vivo*, meningeal CX3CR1(+) cells showed robust migration within the hydrogel matrix, which was not observed with the silicone sealant (supplementary movie 2; figure 7(a), migrating cells denoted by white "*"). Side projection images of this craniotomy confirm that cell and dye infiltration is occurring within the PEG/PEI gel, but not the silicone sealant (figure 7(b)). These side projections also confirm that there is not a significant degree of swelling for this gel as compared to previous reports 30% PEG/PEG cross-linked gels [52]. The size and velocity of cells migrating through the gel between 1–14dpi were quantified (figure 7(c) and (d), 3–5 cells per time point). Cells appear to have slightly elevated velocity compared to cell migration along the electrode's surface at 0.5–1dpi, but similar diameter (figure 2(c)).

4. Discussion

4.1. The meningeal inflammation timeline

A critical step in designing prevention and mitigation strategies for meningeal encapsulation is to understand its time course and progression. We used *in vivo* microscopy to track both CX3CR1(+) meningeal inflammatory cell dynamics as well as meningeal tissue growth. Importantly, the CX3CR1-GFP has expression in most circulating leukocytes (monocytes, dendritic cells, NK cells) as well as tissue macrophage/microglia and some lymphocytes. While this limits our ability to specifically identify cell types throughout our analysis, it provides a comprehensive view of cellular infiltration in the meninges. We show that there is a meningeal reaction to implanted electrodes within the first hours after implantation. This initial reaction consists of rapid cell migration along the surface of the device, as well as cell migration through or along the inner wall of pial venules. Meningeal cell migration speeds along the electrode are >60X faster than microglial migration rates toward the probe, potentially providing a fast attack mechanism to the implant [61]. This is not surprising, as cell migration along a planar surface (such as the meninges) can proceed at much faster rates than through a volume (such as the brain parenchyma)[69]. Interestingly, this migration is transient, and drastically decreases after the first day post-implant. Others have reported that leukocyte migration through venules occurs within the first hour after cortical injury [67]. While their work did not follow leukocyte migration past 16h post-implant, a separate study found that there are normal levels of circulating leukocyte counts by 2 weeks after intracortical electrode implantation, but it is unclear how much earlier normalization could have occurred [12]. This early migratory window likely represents inflammatory mobilization to the craniotomy and implant site as the initiation of wound healing [30]. It is also possible that some of the cells migrating along the electrode's surface are entering the brain. Ravikumar et al., have reported that by 2 weeks post implant, over 60% of macrophage at the intracortical tissue-electrode interface are from peripheral sources [12]. Future studies should focus on determining if the migrating cell population identified in the current study is contributing to intracortical macrophage aggregation.

While the initial migratory window subsided within the first day after implant, meningeal inflammation continued to progress over the next weeks. We observed stable, but variable, cell densities in the meningeal tissue surrounding the device throughout the implantation period. The high variability may be on account to variable vascular damage due to implantation [70]. While we did note variable amounts of vascular dye leakage after implantation, we were unable to clearly visualize vascular damage around the implant due to lack of dye perfusion into damaged vessels. There was persistent remodeling of the meninges over the first 2 weeks. Implants in craniotomies with silicone sealant were held in place and remained protruding through the meninges for the duration of the experiment. This was not the case for implants in craniotomies without a silicone sealant to fix the implant in place. These devices were completely encapsulated and buried in CX3CR1(+) cells by 7–14 days post-implant. It is unclear whether this is due to meningeal cell proliferation, sinking of the brain's surface after surgical edema subsided, or both. Nonetheless, this finding draws concern for probe migration for floating or untethered wireless electrodes.

By two weeks post-implant, the meningeal collagen-I tissue remodeled to be flatter and more conformal to the surface of the electrode. Additionally, the meninges had a significant change in thickness that was independent of sealant condition. This is roughly on par with the time course of encapsulation and ejection of 4×4 Utah arrays in rats, which can happen within 3 months post-implant [37, 38]. In the present study, we show that fibrous tissue remodeling becomes statistically observable only after the first week of implantation and 28 dpi, which is after we observed the peak of meningeal inflammatory cell migration and adhesion to the electrode shank. This sequence of events is corroborated by other studies showing that macrophage presence on foreign bodies is a necessary precursor to fibrous encapsulation [71]. While CX3CR1-GFP expresses in multiple cell types (macrophage, NK cells, dendritic cells, and neutrophils), the immobile, irregularly shaped cells at the meningeal-electrode interface by 7dpi are morphologically consistent with Iba-1(+) macrophage found on foreign bodies in the meninges [41, 52]. This may suggest that the inflammatory immobilization during the migratory window is instrumental for the meningeal remodeling observed at later time points.

4.2. Disambiguating effects of implant, sealant, and craniotomy

During the migratory window in the first days after implantation, the electrode is targeted by meningeal inflammation. The craniotomy may be an underappreciated contributor to the inflammatory response when compared to the implantation injury and the foreign body response. It is possible that the electrode is merely a bystander during the broader wound healing response of bone healing. In support of this, craniotomy alone has been implicated in cognitive impairment as well as transient elevation of inflammatory cytokines, astrocyte markers, phagocytosis markers, and antigen presenting cells to a similar degree as traumatic brain injury in a mouse model [72–74]. Craniotomy can also lead to significant meningeal thickening in both rabbit and dog models [75, 76]. These effects can also be modulated by the size of the craniotomy [77, 78]. The large craniotomies used in this study are considered "critical-size" cranial defects in mice, which result in poor bone regrowth and meningeal thickening [35, 79]. Smaller craniotomies would have likely resulted in faster bone growth

over the craniotomy and potentially altered meningeal inflammation and wound healing. While smaller craniotomies in neural engineering are often used in small animal models, large device implantations in non-human primate and clinical populations often use substantial craniotomies > 16cm^2 that are considered critical sized in human [21, 31, 32]. Further, while these larger craniotomies are often sealed with autologous bone graft, defects of this scale can suffer from poor bone graft integration [32]. This suggests that, while the critical-sized defect used in this study may have been a factor in the meningeal response, it is a scaled model for clinical deployments of neural implants. Future studies can probe the effect of the craniotomy by examining meningeal encapsulation in craniotomies of varying sizes or by allowing the craniotomy to heal to before device implantation. Polymeric and growth-factor loaded scaffolds have also been effective in improving wound healing after critical-sized cranial defects and therefore should also be pursued to modulate craniotomy-effects in neural implant biocompatibility [33–35, 80].

Surgical preparation may also have an impact on the formation of fibrous tissue. In this study as in other mouse studies, the electrode was implanted through the very thin dura (~20 μm thick, see figure 5) [17]. Larger animals typically have thicker dura (>300 μm in rhesus macaque) that is typically reflected prior to insertion and then sutured back in place [21, 41]. This additional intervention in the meninges may lead to exacerbated meningeal encapsulation as hemorrhage [28, 29] and mechanical trauma [30] in the meninges are both known to increase inflammatory mobilization and collagen synthesis within the meninges. Despite this, epi-durally implanted ECoG grids also generate a significant encapsulation response, suggesting that the effects from craniotomy and/or chronic foreign body placement are sufficient to generate a response [42, 43].We have also previously noted that the silicone sealant material can generate its own foreign body response [52]. We controlled for this by tracking meningeal remodeling in a cohort of implantations into craniotomies with no sealant. There were similar levels meningeal thickening with or without the sealant. Without the sealant to fix the implant in place, however, the device became buried in meningeal tissue. As an alternative to a “no-sealant” condition, choosing a different sealant or dural graft material can impact the degree of fibrotic response [75, 76, 81]. We examined the meningeal inflammatory response to anon-degradable PEG/PEI gel that is similar to commercially available resorbable PEG-based gels [68, 76]. The PEG/PEI gel had rapid inflammatory cell infiltration within the gel, which was not observed in the silicone sealant. This may be due to the hydrophilicity and high pore size of low-molecular weight PEG-based hydrogels, which promotes infiltration [82]. Previous reports have shown that cellular infiltration may promote more rapid wound healing, but it is unclear how rapid wound healing would interact with meningeal encapsulation of neural implants [83]. Cell infiltration may have additional implications for drug-eluting hydrogels, where infiltrating cells related to inflammation and wound healing would be exposed to the highest concentration of drug within the gel [84]. As a case study of the PEG/PEI gel, these results show that cellular infiltration is possible in hydrogel sealant materials, but these results cannot be generalized to PEG/PEI or other hydrogel materials. Future studies should further explore the interaction of hydrogel materials and meningeal inflammation, as well as optimizing pore size, hydrophilicity, and degradation to identify a superior sealant material [85, 86].

4.3. Relevance for fibrous implant ejection in high order animals

These results show that there is a consistent meningeal response in the first month of implantation for mice. There is a similarly consistent, fibrous reaction to implants in rats and cats [19, 37, 38]. In non-human primates, however, there are no studies that track progression of meningeal encapsulation, only reports on when devices have failed from meningeal encapsulation (21–261 days post implant for 9 devices) [21, 36]. It is likely that there is progressive increase of encapsulation leading to that failure point. Electrical impedance spectroscopy may provide some *in vivo* monitoring of encapsulation. Some groups have reported trends of decreasing electrical impedance for Utah style electrodes that are encapsulated and ejected from the brain [36, 37]. This may be due to the cone-shape of the Utah array shank. As the electrode site is pushed up through the cone-shaped tract, there would be an increasing gap between the electrode surface and the surrounding tissue that could lead to lower impedance. Decreasing impedance could also be explained by electrode insulation delamination and electrode site shortage, and so cannot be considered a unique signature for meningeal encapsulation and ejection [37, 87].

While the meningeal thickening observed in the current study appears to be uniform throughout the craniotomy, we observed that collagen at the meningeal-electrode interface grew to be more conformal to the face of the electrode. This is similar to10×10 Utah arrays in non-human primates, where fibrous growth appears to conform around the exterior of the device (figure 8) [36]. In explanted devices from these higher order animals, collagen-I signal often appears to tightly follow the edge of the device's platform (figure 8(b)). While we observe similarities in collagen remodeling behavior between these models, conformal encapsulation of the larger Utah arrays is more often identified as a source of failure than for planar style devices. This may be partly due to the large 2D platform that is present on the Utah array. The presence of a large 2D platform even without penetrating shanks—such as an ECoG grid—is sufficient to elicit a meningeal encapsulation response [41–44]. Notably, in the Utah array, the gold wire that bridge the connector and the platform are potted with medical-grade silicone, and may generate a similar meningeal reaction as the silicone sealant [52] or silicone platform ECoG grids [41, 44]. To interrogate the role of the platform footprint and material as well as the non-human primate meningeal response, controlled histological studies with discrete end-points should be conducted.

4.4. Mitigation strategies and future directions

Preventing meningeal fibrosis is a major obstacle to wide-spread translation of brain-computer interface technologies. We have shown that there is a migratory window in the first days after implant that precedes meningeal fibrosis. With the CX3CR1-GFP model, we were able to survey a broad scope of inflammatory cell activity, but were unable to identify whether migrating cells were myeloid, neutrophil, dendritic, or NK cells. Future studies should either use more cell-specific models or post-mortem histology to further identify cell types, as this could be useful in defining therapeutics and further understanding the relationship between migration and fibrosis. Another way to elucidate the relationship between these phenomena is to modulate that initial migratory window. Roth et al. have shown that anti-inflammatory therapeutics as well as purinergic signaling inhibitors are viable routes to modulate acute meningeal inflammation [30]. Cell adhesion to the electrode

shanks, electrode array platforms, and dural sealants and grafts may also serve as a critical precursor to encapsulation. Macrophage and fibroblast adhesion to substrates can be modulated by surface treatments of L1 cell adhesion molecule [58, 88–91] as well as different polymeric surfaces [92]. Inflammatory macrophage behavior can also be modulated with controlled-drug release from meningeal-interfacing domains of implants [51, 93–97]. Anti-fibrotic medication may also be a viable target [98].

On a macroscale, the surgical preparation and device design may also have critical repercussions for meningeal inflammation and encapsulation. The precision and size of craniotomies affects the amount of post-operative inflammation [73, 77] and choice of dural repair method and material can have an impact on the amount of meningeal fibrosis [75, 81]. To our knowledge, there have been no controlled optimization studies for these parameters. The presence of a 2D platform in the meninges may also govern the fibrotic response. Advances in ECoG devices can be emulated to pursue mesh style platforms [42] and flexible platforms [99–101] to reduce meningeal encapsulation of neural electrodes.

5. Conclusions

With cell migration speeds 60X faster than the cortex, the meningeal response to implanted electrode devices may be a “fast attack” mechanism. A transient, migratory window of cell infiltration to the electrode precedes meningeal remodeling at later timepoints. This migratory window may provide a critical therapeutic target for reducing long-term meningeal encapsulation.

Supplementary Material

Refer to Web version on PubMed Central for supplementary material.

Acknowledgments

This project was financially supported by NIH NINDS (Grant R01NS062019, R01NS094396, R01NS089688, R01NS094404). The authors thank the Motorlab, directed by Dr. Andrew Schwartz, at University of Pittsburgh for donating non-human primate tissue and Dr. Yijen Wu, director of the Animal Imaging Core at Rangos Research Center at Children’s Hospital of Pittsburgh of UPMC, for assistance in microCT imaging.

References

[1]. Schwartz AB, Cortical neural prosthetics., Annual review of neuroscience 27 (2004) 487–507.

[2]. Schwartz AB, Cui XT, Weber DJ, Moran DW, Brain-controlled interfaces: movement restoration with neural prosthetics., Neuron 52 (2006) 205–20. [PubMed: 17015237]

[3]. Kipke DR, Shain W, Buzsaki G, Fetz E, Henderson JM, Hetke JF, Schalk G, Advanced Neurotechnologies for Chronic Neural Interfaces: New Horizons and Clinical Opportunities, Journal of Neuroscience 28 (2008) 11830–11838. [PubMed: 19005048]

[4]. Brandman DM, Cash SS, Hochberg LR, Review: Human Intracortical recording and neural decoding for brain-computer interfaces, IEEE Trans Neural Syst Rehabil Eng (2017).

[5]. Iordanova B, Vazquez AL, Kozai TDY, Fukuda M, Kim SG, Optogenetic investigation of the variable neurovascular coupling along the interhemispheric circuits Journal of Cerebral Blood Flow & Metabolism 38(4) (2018) 627–640. [PubMed: 29372655]

[6]. Michelson NJ, Kozai TDY, Isoflurane and Ketamine Differentially Influence Spontaneous and Evoked Laminar Electrophysiology in Mouse V1, J Neurophysiol (2018).

[7]. Michelson NJ, Eles JR, Vazquez AL, Ludwig KA, Kozai TDY, Calcium activation of cortical neurons by continuous electrical stimulation: Frequency-dependence, temporal fidelity and activation density, Journal of neuroscience research Accepted (2018).

[8]. Flesher SN, Collinger JL, Foldes ST, Weiss JM, Downey JE, Tyler-Kabara EC, Bensmaia SJ, Schwartz AB, Boninger ML, Gaunt RA, Intracortical microstimulation of human somatosensory cortex, Science Translational Medicine (2016) aaf8083.

[9]. McConnell GC, Rees HD, Levey AI, Gutekunst C-A, Gross RE, Bellamkonda RV, Implanted neural electrodes cause chronic, local inflammation that is correlated with local neurodegeneration., Journal of neural engineering 6 (2009) 056003. [PubMed: 19700815]

[10]. Potter KA, Buck AC, Self WK, Capadona JR, Stab injury and device implantation within the brain results in inversely multiphasic neuroinflammatory and neurodegenerative responses, J Neural Eng 9(4) (2012) 046020. [PubMed: 22832283]

[11]. Biran R, Martin DC, Tresco PA, Neuronal cell loss accompanies the brain tissue response to chronically implanted silicon microelectrode arrays, Experimental Neurology 195 (2005) 115–126. [PubMed: 16045910]

[12]. Ravikumar M, Sunil S, Black J, Barkauskas DS, Haung AY, Miller RH, Selkirk SM, Capadona JR, The roles of blood-derived macrophages and resident microglia in the neuroinflammatory response to implanted intracortical microelectrodes., Biomaterials 35 (2014) 8049–64. [PubMed: 24973296]

[13]. Wellman SM, Kozai TDY, Understanding the Inflammatory Tissue Reaction to Brain Implants To Improve Neurochemical Sensing Performance, ACS Chemical Neuroscience (2017).

[14]. Kozai TDY, Jaquins-Gerstl A, Vazquez AL, Michael AC, Cui XT, Brain Tissue Responses to Neural Implants Impact Signal Sensitivity and Intervention Strategies, ACS Chemical Neuroscience 6(1) (2015) 48–67. [PubMed: 25546652]

[15]. Kozai TDY, Gugel Z, Li X, Gilgunn PJ, Khilwani R, Ozdoganlar OB, Fedder GK, Weber DJ, Cui XT, Chronic tissue response to carboxymethyl cellulose based dissolvable insertion needle for ultra-small neural probes, Biomaterials 35(34) (2014) 9255–68. [PubMed: 25128375]

[16]. Wellman SM, Kozai TDY, In vivo spatiotemporal dynamics of NG2 glia activity caused by neural electrode implantation, Biomaterials 164 (2018) 121–133. [PubMed: 29501892]

[17]. Kozai TDY, Li X, Bodily LM, Caparosa EM, Zenonos GA, Carlisle DL, Friedlander RM, Cui XT, Effects of caspase-1 knockout on chronic neural recording quality and longevity: insight into cellular and molecular mechanisms of the reactive tissue response., Biomaterials 35 (2014) 9620–34. [PubMed: 25176060]

[18]. Kozai TDY, Du Z, Gugel ZV, Smith MA, Chase SM, Bodily LM, Caparosa EM, Friedlander RM, Cui XT, Comprehensive chronic laminar single-unit, multi-unit, and local field potential recording performance with planar single shank electrode arrays, Journal of Neuroscience Methods 242(1) (2015) 15–40. [PubMed: 25542351]

[19]. Rousche PJ, Normann RA, Chronic recording capability of the Utah Intracortical Electrode Array in cat sensory cortex, J Neurosci Methods 82(1) (1998) 1–15. [PubMed: 10223510]

[20]. Chestek CA, Gilja V, Nuyujukian P, Foster JD, Fan JM, Kaufman MT, Churchland MM, Rivera-Alvidrez Z, Cunningham JP, Ryu SI, Shenoy KV, Long-term stability of neural prosthetic control signals from silicon cortical arrays in rhesus macaque motor cortex., Journal of neural engineering 8 (2011) 045005. [PubMed: 21775782]

[21]. Barrese JC, Rao N, Paroo K, Triebwasser C, Vargas-Irwin C, Franquemont L, Donoghue JP, Failure mode analysis of silicon-based intracortical microelectrode arrays in non-human primates., Journal of neural engineering 10 (2013) 066014. [PubMed: 24216311]

[22]. Wellman SM, Eles JR, Ludwig KA, Seymour JP, Michelson NJ, McFadden WE, Vazquez AL, Kozai TDY, A Materials Roadmap to Functional Neural Interface Design, Advanced Functional Materials 1701269-n/a.

[23]. Wright BL, Lai JT, Sinclair AJ, Cerebrospinal fluid and lumbar puncture: a practical review, Journal of neurology 259(8) (2012) 1530–45. [PubMed: 22278331]

[24]. Zhang ET, Inman CB, Weller RO, Interrelationships of the pia mater and the perivascular (Virchow-Robin) spaces in the human cerebrum., Journal of anatomy 170 (1990) 111–23. [PubMed: 2254158]

[25]. Plog BA, Nedergaard M, The glymphatic system in CNS health and disease: past, present and future, Annual review of pathology 13 (2018) 379–394.

[26]. Bartholomäus I, Kawakami N, Odoardi F, Schläger C, Miljkovic D, Ellwart JW, Klinkert WEF, Flügel-Koch C, Issekutz TB, Wekerle H, Flügel A, Effector T cell interactions with meningeal vascular structures in nascent autoimmune CNS lesions., Nature 462 (2009) 94–98. [PubMed: 19829296]

[27]. Cha J-H, Wee H-J, Seo JH, Ahn BJ, Park J-H, Yang J-M, Lee S-W, Lee O-H, Lee H-J, Gelman IH, Arai K, Lo EH, Kim K-W, Prompt meningeal reconstruction mediated by oxygen-sensitive AKAP12 scaffolding protein after central nervous system injury., Nature communications 5 (2014) 4952.

[28]. Lindsberg PJ, Strbian D, Karjalainen-Lindsberg M-L, Mast cells as early responders in the regulation of acute blood-brain barrier changes after cerebral ischemia and hemorrhage., Journal of cerebral blood flow and metabolism : official journal of the International Society of Cerebral Blood Flow and Metabolism 30 (2010) 689–702.

[29]. Sajanti J, Bjorkstrand AS, Finnila S, Heikkinen E, Peltonen J, Majamaa K, Increase of collagen synthesis and deposition in the arachnoid and the dura following subarachnoid hemorrhage in the rat, Biochimica et biophysica acta 1454(3) (1999) 209–16. [PubMed: 10452955]

[30]. Roth TL, Nayak D, Atanasijevic T, Koretsky AP, Latour LL, McGavern DB, Transcranial amelioration of inflammation and cell death after brain injury., Nature 505 (2014) 223–8. [PubMed: 24317693]

[31]. Mégevand P, Woodtli A, Yulzari A, Cosgrove GR, Momjian S, Stimec BV, Corniola MV, Fasel JHD, Surgical Training for the Implantation of Neocortical Microelectrode Arrays Using a Formaldehyde-fixed Human Cadaver Model, JoVE (129) (2017) e56584.

[32]. Goldstein JA, Paliga JT, Bartlett SP, Cranioplasty: indications and advances, Current Opinion in Otolaryngology & Head and Neck Surgery 21(4) (2013) 400–409. [PubMed: 23770828]

[33]. Humber CC, Sandor GK, Davis JM, Peel SA, Brkovic BM, Kim YD, Holmes HI, Clokie CM, Bone healing with an in situ-formed bioresorbable polyethylene glycol hydrogel membrane in rabbit calvarial defects, Oral surgery, oral medicine, oral pathology, oral radiology, and endodontics 109(3) (2010) 372–84.

[34]. Spicer PP, Kretlow JD, Young S, Jansen JA, Kasper FK, Mikos AG, Evaluation of bone regeneration using the rat critical size calvarial defect, Nature protocols 7(10) (2012) 1918–1929. [PubMed: 23018195]

[35]. Terella A, Mariner P, Brown N, Anseth K, Streubel S-O, Repair of a calvarial defect with biofactor and stem cell-embedded polyethylene glycol scaffold, Archives of facial plastic surgery 12(3) (2010) 166–171. [PubMed: 20479432]

[36]. Barrese JC, Aceros J, Donoghue JP, Scanning electron microscopy of chronically implanted intracortical microelectrode arrays in non-human primates, J Neural Eng 13(2) (2016) 026003. [PubMed: 26824680]

[37]. Cody PA, Eles JR, Lagenaur CF, Kozai TDY, Cui XT, Unique electrophysiological and impedance signatures between encapsulation types: An analysis of biological Utah array failure and benefit of a biomimetic coating in a rat model, Biomaterials 161 (2018) 117–128. [PubMed: 29421549]

[38]. Nolta NF, Christensen MB, Crane PD, Skousen JL, Tresco PA, BBB leakage, astrogliosis, and tissue loss correlate with silicon microelectrode array recording performance, Biomaterials 53 (2015) 753–762. [PubMed: 25890770]

[39]. Anderson JM, Rodriguez A, Chang DT, Foreign body reaction to biomaterials, Seminars in Immunology 20 (2008) 86–100. [PubMed: 18162407]

[40]. Anderson JM, Biological Responses to Materials, Annual Review of Materials Research 31(1) (2001) 81–110.

[41]. Degenhart AD, Eles J, Dum R, Mischel JL, Smalianchuk I, Endler B, Ashmore RC, Tyler-Kabara EC, Hatsopoulos NG, Wang W, Batista AP, Cui XT, Histological evaluation of a chronically-implanted electrocorticographic electrode grid in a non-human primate., Journal of neural engineering 13 (2016) 046019. [PubMed: 27351722]

[42]. Schendel A.a., Nonte MW, Vokoun C, Richner TJ, Brodnick SK, Atry F, Frye S, Bostrom P, Pashaie R, Thongpang S, Eliceiri KW, Williams JC, The effect of micro-ECoG substrate footprint on the meningeal tissue response., Journal of neural engineering 11 (2014) 046011. [PubMed: 24941335]

[43]. Schendel AA, Thongpang S, Brodnick SK, Richner TJ, Lindevig BDB, Krugner-Higby L, Williams JC, A cranial window imaging method for monitoring vascular growth around chronically implanted micro-ECoG devices, Journal of Neuroscience Methods 218 (2013) 121–130. [PubMed: 23769960]

[44]. Henle C, Raab M, Cordeiro JG, Doostkam S, Schulze-Bonhage A, Stieglitz T, Rickert J, First long term in vivo study on subdurally implanted Micro-ECoG electrodes, manufactured with a novel laser technology, Biomedical Microdevices 13(1) (2011) 59–68. [PubMed: 20838900]

[45]. Kim Y-T, Hitchcock RW, Bridge MJ, Tresco PA, Chronic response of adult rat brain tissue to implants anchored to the skull., Biomaterials 25 (2004) 2229–37. [PubMed: 14741588]

[46]. Markwardt NT, Stokol J, Rennaker RL, II, Sub-meninges implantation reduces immune response to neural implants., Journal of neuroscience methods 214 (2013) 119–25. [PubMed: 23370311]

[47]. Biran R, Martin DC, Tresco PA, The brain tissue response to implanted silicon microelectrode arrays is increased when the device is tethered to the skull, Journal of Biomedical Materials Research Part A 82A (2007) 169–178.

[48]. Woolley AJ, Desai HA, Otto KJ, Chronic intracortical microelectrode arrays induce non-uniform, depth-related tissue responses., Journal of neural engineering 10 (2013) 026007. [PubMed: 23428842]

[49]. Maynard EM, Fernandez E, Normann RA, A technique to prevent dural adhesions to chronically implanted microelectrode arrays, Journal of Neuroscience Methods 97(2) (2000) 93–101. [PubMed: 10788663]

[50]. Spitler KM, Gothard KM, A removable silicone elastomer seal reduces granulation tissue growth and maintains the sterility of recording chambers for primate neurophysiology, Journal of Neuroscience Methods 169(1) (2008) 23–26. [PubMed: 18241928]

[51]. Spinks RL, Baker SN, Jackson A, Khaw PT, Lemon RN, Problem of dural scarring in recording from awake, behaving monkeys: a solution using 5-fluorouracil, J Neurophysiol 90(2) (2003) 1324–32. [PubMed: 12904511]

[52]. Kozai TDY, Eles JR, Vazquez AL, Cui XT, Two-photon imaging of chronically implanted neural electrodes: Sealing methods and new insights, Journal of Neuroscience Methods 258 (2016) 46–55. [PubMed: 26526459]

[53]. Jung S, Aliberti J, Graemmel P, Sunshine MJ, Kreutzberg GW, Sher A, Littman DR, Analysis of Fractalkine Receptor CX(3)CR1 Function by Targeted Deletion and Green Fluorescent Protein Reporter Gene Insertion, Molecular and Cellular Biology 20(11) (2000) 4106–4114. [PubMed: 10805752]

[54]. Stockman K, Carnahan M, D'Alessio K, Grinstaff M, Crosslinked gels comprising polyalkyleneimines, and their uses as medical devices, Square 1 Bank USA, 2007.

[55]. Catt K, Li H, Cui XT, Poly (3,4-ethylenedioxythiophene) graphene oxide composite coatings for controlling magnesium implant corrosion, Acta Biomaterialia 48 (2017) 530–540. [PubMed: 27867108]

[56]. Catt K, Li H, Hoang V, Beard R, Cui XT, Self-powered therapeutic release from conducting polymer/graphene oxide films on magnesium, Nanomedicine: Nanotechnology, Biology and Medicine (2017).

[57]. Luo X, Matranga C, Tan S, Alba N, Cui XT, Carbon nanotube nanoreservior for controlled release of anti-inflammatory dexamethasone., Biomaterials 32 (2011) 6316–23. [PubMed: 21636128]

[58]. Eles JR, Vazquez AL, Snyder NR, Lagenaur CF, Murphy MC, Kozai TDY, Cui XT, Neuroadhesive L1 coating attenuates acute microglial attachment to neural electrodes as revealed by live two-photon microscopy, Biomaterials 113 (2017) 279–292. [PubMed: 27837661]

[59]. Eles JR, Vazquez AL, Kozai TDY, Cui XT, In vivo imaging of neuronal calcium during electrode implantation: Spatial and temporal mapping of damage and recovery, Biomaterials 174 (2018) 79–94. [PubMed: 29783119]

[60]. Thevenaz P, Ruttimann UE, Unser M, A pyramid approach to subpixel registration based on intensity, IEEE Transactions on Image Processing 7 (1998) 27–41. [PubMed: 18267377]

[61]. Wellman SM, Kozai TDY, In vivo spatiotemporal dynamics of NG2 glia activity caused by neural electrode implantation, Biomaterials 164 (2018) 121–133. [PubMed: 29501892]

[62]. Ridler T, Calvard S, Picture Thresholding Using an Iterative Selection Method, IEEE Transactions on Systems, Man, and Cybernetics 8 (1978) 630–632.

[63]. Kozai TDY, Jaquins-Gerstl AS, Vazquez AL, Michael AC, Cui XT, Brain Tissue Responses to Neural Implants Impact Signal Sensitivity and Intervention Strategies, ACS Chemical Neuroscience 6 (2015) 48–67. [PubMed: 25546652]

[64]. Hammer DX, Lozzi A, Abliz E, Greenbaum N, Agrawal A, Krauthamer V, Welle CG, Longitudinal vascular dynamics following cranial window and electrode implantation measured with speckle variance optical coherence angiography, Biomedical Optics Express 5(8) (2014) 2823–2836. [PubMed: 25136505]

[65]. Rovainen CM, Woolsey TA, Blocher NC, Wang D-B, Robinson OF, Blood Flow in Single Surface Arterioles and Venules on the Mouse Somatosensory Cortex Measured with Videomicroscopy, Fluorescent Dextrans, Nonoccluding Fluorescent Beads, and Computer-Assisted Image Analysis, Journal of Cerebral Blood Flow & Metabolism 13(3) (1993) 359–371. [PubMed: 7683023]

[66]. Ritter LS, Orozco JA, Coull BM, McDonagh PF, Rosenblum WI, Leukocyte accumulation and hemodynamic changes in the cerebral microcirculation during early reperfusion after stroke, Stroke 31(5) (2000) 1153–61. [PubMed: 10797180]

[67]. Schwarzmaier SM, Zimmermann R, McGarry NB, Trabold R, Kim SW, Plesnila N, In vivo temporal and spatial profile of leukocyte adhesion and migration after experimental traumatic brain injury in mice, J Neuroinflammation 10 (2013) 32. [PubMed: 23448240]

[68]. Zoia C, Bongetta D, Lombardi F, Custodi VM, Pugliese R, Gaetani P, First Impressions about Adherus, a New Dural Sealant, Journal of Applied Biomaterials & Functional Materials 13(4) (2015) 372–375.

[69]. Vu LT, Jain G, Veres BD, Rajagopalan P, Cell Migration on Planar and Three-Dimensional Matrices: A Hydrogel-Based Perspective, Tissue Engineering. Part B, Reviews 21(1) (2015) 67–74. [PubMed: 25011932]

[70]. Kozai TDY, Marzullo TC, Hooi F, Langhals NB, Majewska AK, Brown EB, Kipke DR, Reduction of neurovascular damage resulting from microelectrode insertion into the cerebral cortex using in vivo two-photon mapping., Journal of neural engineering 7 (2010) 046011. [PubMed: 20644246]

[71]. Doloff JC, Veiseh O, Vegas AJ, Tam HH, Farah S, Ma M, Li J, Bader A, Chiu A, Sadraei A, Aresta-Dasilva S, Griffin M, Jhunjhunwala S, Webber M, Siebert S, Tang K, Chen M, Langan E, Dholokia N, Thakrar R, Qi M, Oberholzer J, Greiner DL, Langer R, Anderson DG, Colony stimulating factor-1 receptor is a central component of the foreign body response to biomaterial implants in rodents and non-human primates, Nature Materials 16 (2017) 671. [PubMed: 28319612]

[72]. Lagraoui M, Latoche JR, Cartwright NG, Sukumar G, Dalgard CL, Schaefer BC, Controlled Cortical Impact and Craniotomy Induce Strikingly Similar Profiles of Inflammatory Gene Expression, but with Distinct Kinetics, Frontiers in Neurology 3 (2012) 155. [PubMed: 23118733]

[73]. Cole JT, Yarnell A, Kean WS, Gold E, Lewis B, Ren M, McMullen DC, Jacobowitz DM, Pollard HB, O'Neill JT, Grunberg NE, Dalgard CL, Frank JA, Watson WD, Craniotomy: True Sham for Traumatic Brain Injury, or a Sham of a Sham?, Journal of Neurotrauma 28(3) (2011) 359–369. [PubMed: 21190398]

[74]. Sashindranath M, Daglas M, Medcalf RL, Evaluation of gait impairment in mice subjected to craniotomy and traumatic brain injury, Behavioural brain research 286 (2015) 33–8. [PubMed: 25721743]

[75]. Nunamaker EA, Kipke DR, An alginate hydrogel dura mater replacement for use with intracortical electrodes, J Biomed Mater Res B Appl Biomater 95(2) (2010) 421–9. [PubMed: 20878928]

[76]. Preul MC, Bichard WD, Muench TR, Spetzler RF, Toward Optimal Tissue Sealants for Neurosurgery: Use of a Novel Hydrogel Sealant in a Canine Durotomy Repair Model, Neurosurgery 53(5) (2003) 1189–1199. [PubMed: 14580287]

[77]. Forcelli PA, Kalikhman D, Gale K, Delayed effect of craniotomy on experimental seizures in rats, PLoS One 8(12) (2013) e81401. [PubMed: 24324691]

[78]. Szpalski C, Barr J, Wetterau M, Saadeh PB, Warren SM, Cranial bone defects: current and future strategies, Neurosurg Focus 29(6) (2010) E8.

[79]. Cooper GM, Mooney MP, Gosain AK, Campbell PG, Losee JE, Huard J, Testing the critical size in calvarial bone defects: revisiting the concept of a critical-size defect, Plastic and reconstructive surgery 125(6) (2010) 1685–1692. [PubMed: 20517092]

[80]. Hopper RA, Zhang JR, Fourasier VL, Morova-Protzner I, Protzner KF, Pang CY, Forrest CR, Effect of isolation of periosteum and dura on the healing of rabbit calvarial inlay bone grafts, Plastic and reconstructive surgery 107(2) (2001) 454–62. [PubMed: 11214061]

[81]. Barbolt TA, Odin M, Leger M, Kangas L, Hoiste J, Liu SH, Biocompatibility evaluation of dura mater substitutes in an animal model, Neurological research 23(8) (2001) 813–20. [PubMed: 11760872]

[82]. Singh A, Suri S, Roy K, In-situ crosslinking hydrogels for combinatorial delivery of chemokines and siRNA-DNA carrying microparticles to dendritic cells, Biomaterials 30(28) (2009) 5187. [PubMed: 19560815]

[83]. Zhao X, Sun X, Yildirimer L, Lang Q, Lin ZYW, Zheng R, Zhang Y, Cui W, Annabi N, Khademhosseini A, Cell infiltrative hydrogel fibrous scaffolds for accelerated wound healing, Acta Biomater 49 (2017) 66–77. [PubMed: 27826004]

[84]. Hoare TR, Kohane DS, Hydrogels in drug delivery: Progress and challenges, Polymer 49(8) (2008) 1993–2007.

[85]. Jo S, Kang SM, Park SA, Kim WD, Kwak J, Lee H, Enhanced adhesion of preosteoblasts inside 3D PCL scaffolds by polydopamine coating and mineralization, Macromol Biosci 13(10) (2013) 1389–95. [PubMed: 23861256]

[86]. Baker BM, Gee AO, Metter RB, Nathan AS, Marklein RA, Burdick JA, Mauck RL, The potential to improve cell infiltration in composite fiber-aligned electrospun scaffolds by the selective removal of sacrificial fibers, Biomaterials 29(15) (2008) 2348–58. [PubMed: 18313138]

[87]. Kozai TDY, Catt K, Li X, Gugel ZV, Olafsson VT, Vazquez AL, Cui XT, Mechanical failure modes of chronically implanted planar silicon-based neural probes for laminar recording, Biomaterials 37 (2015) 25–39. [PubMed: 25453935]

[88]. Azemi E, Lagenaur CF, Cui XT, The surface immobilization of the neural adhesion molecule L1 on neural probes and its effect on neuronal density and gliosis at the probe/tissue interface., Biomaterials 32 (2011) 681–92. [PubMed: 20933270]

[89]. Azemi E, Stauffer WR, Gostock MS, Lagenaur CF, Cui XT, Surface immobilization of neural adhesion molecule L1 for improving the biocompatibility of chronic neural probes: In vitro characterization., Acta biomaterialia 4 (2008) 1208–17. [PubMed: 18420473]

[90]. Kolarcik CL, Bourbeau D, Azemi E, Rost E, Zhang L, Lagenaur CF, Weber DJ, Cui XT, In vivo effects of L1 coating on inflammation and neuronal health at the electrode-tissue interface in rat spinal cord and dorsal root ganglion., Acta biomaterialia 8 (2012) 3561–75. [PubMed: 22750248]

[91]. Webb K, Budko E, Neuberger TJ, Chen S, Schachner M, Tresco PA, Substrate-bound human recombinant L1 selectively promotes neuronal attachment and outgrowth in the presence of astrocytes and fibroblasts., Biomaterials 22 (2001) 1017–28. [PubMed: 11352083]

[92]. Manwaring ME, Biran R, Tresco PA, Characterization of rat meningeal cultures on materials of differing surface chemistry, Biomaterials 22(23) (2001) 3155–68. [PubMed: 11603588]

[93]. Kim D-H, Martin DC, Sustained release of dexamethasone from hydrophilic matrices using PLGA nanoparticles for neural drug delivery., Biomaterials 27 (2006) 3031–7. [PubMed: 16443270]

[94]. Kozai TDY, Jaquins-gerstl AS, Vazquez AL, Michael AC, Cui XT, Biomaterials Dexamethasone retrodialysis attenuates microglial response to implanted probes in vivo, Biomaterials 87 (2016) 157–169. [PubMed: 26923363]

[95]. Luo X, Matranga C, Tan S, Alba N, Cui XT, Carbon nanotube nanoreservior for controlled release of anti-inflammatory dexamethasone, Biomaterials 32(26) (2011) 6316–23. [PubMed: 21636128]

[96]. Wadhwa R, Lagenaur CF, Cui XT, Electrochemically controlled release of dexamethasone from conducting polymer polypyrrole coated electrode, Journal of Controlled Release 110 (2006) 531–541. [PubMed: 16360955]

[97]. Zhong Y, Bellamkonda RV, Dexamethasone-coated neural probes elicit attenuated inflammatory response and neuronal loss compared to uncoated neural probes., Brain research 1148 (2007) 15–27. [PubMed: 17376408]

[98]. Rosenbloom J, Mendoza FA, Jimenez SA, Strategies for anti-fibrotic therapies, Biochimica et biophysica acta 1832(7) (2013) 1088–103. [PubMed: 23266403]

[99]. Yamakawa T, Yamakawa T, Aou S, Ishizuka S, Suzuki M, Fujii M, Subdural electrode array manipulated by a shape memory alloy guidewire for minimally-invasive electrocorticogram recording, 2010 World Automation Congress, 2010, pp. 1–6.

[100]. Yeager JD, Phillips DJ, Rector DM, Bahr DF, Characterization of flexible ECoG electrode arrays for chronic recording in awake rats, J Neurosci Methods 173(2) (2008) 279–85. [PubMed: 18640155]

[101]. Kim D-H, Viventi J, Amsden JJ, Xiao J, Vigeland L, Kim Y-S, Blanco JA, Panilaitis B, Frechette ES, Contreras D, Kaplan DL, Omenetto FG, Huang Y, Hwang K-C, Zakin MR, Litt B, Rogers JA, Dissolvable films of silk fibroin for ultrathin conformal bio-integrated electronics, Nature Materials 9 (2010) 511. [PubMed: 20400953]

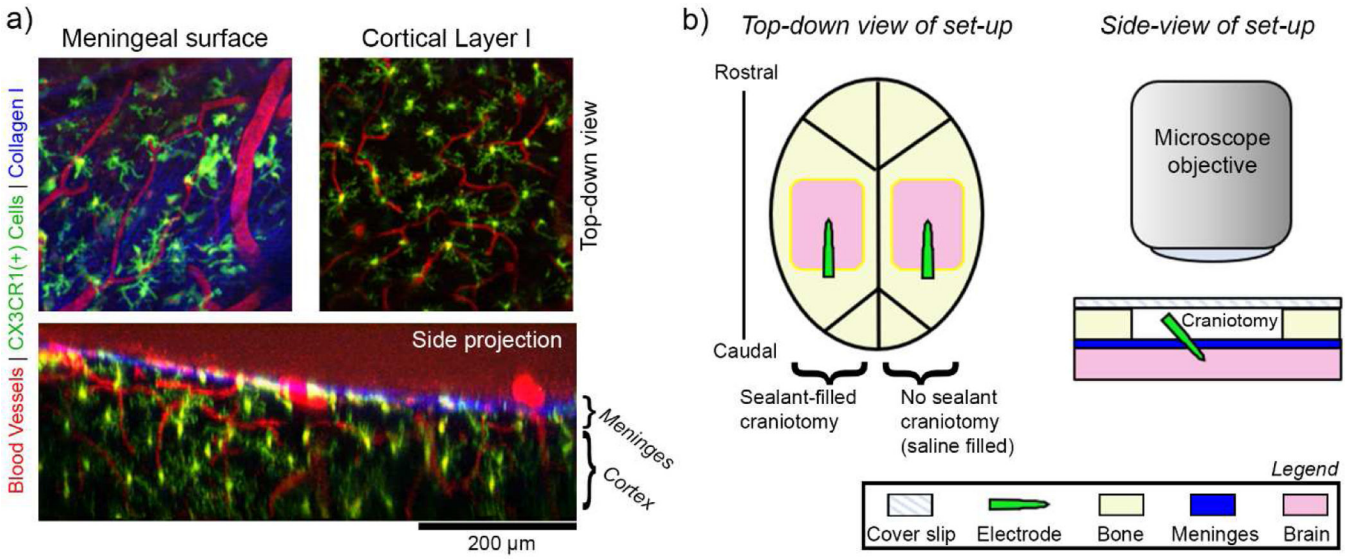

Figure 1.

In vivo imaging of meningeal response to implanted electrode arrays. (a) Example two-photon microscope images of pre-implant meningeal biology in CXCR1-GFP mice. Top-down images of the meninges (top left) and underlying cortex (top right) show distinct collagen I (blue), vascular (red), and CX3CR1(+) cellular morphologies (green). A side projection of the same region shows the spatial relationship between the meningeal and cortical compartments (bottom). The boundary between the meninges and cortex can be defined by the bright blue collagen trace along the surface of the brain. (b) Schematic of the in vivo implantation set-up. Left: Bilateral cranial windows are prepared for each mouse. Craniotomies are either filled a sealant material (silicone elastomer or PEG gel) or saline (no sealant) prior to being covered with a glass cover slip. Right: A cross-section of the set-up highlights that implants are fully underneath the glass coverslip. A two-photon microscope objective can be lowered over the glass coverslip to enable longitudinal imaging.

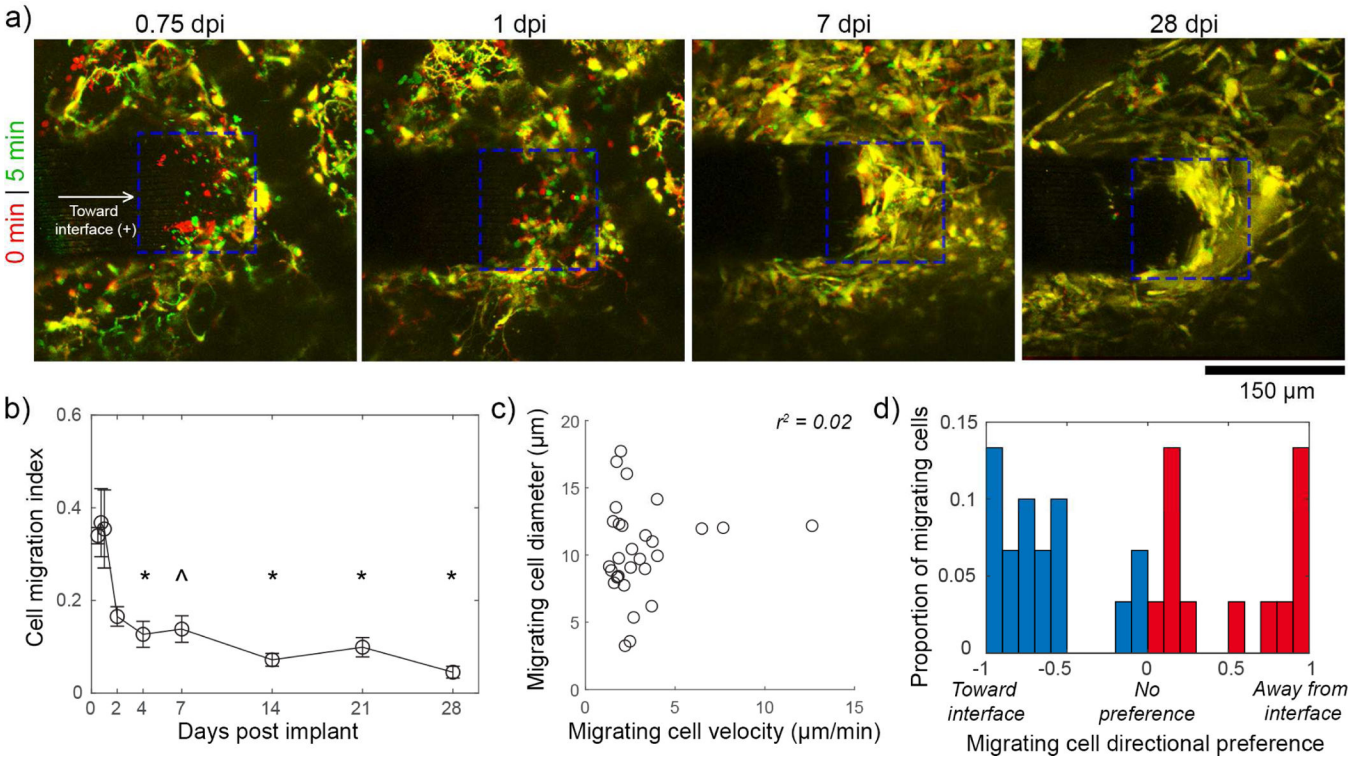

Figure 2.

Meningeal CX3CR1(+) cells migrate along the electrode's surface during the first days post-implant. (a) Superimposed images of the meningeal-electrode interface (ROI denoted by blue dashed box) at earlier (red) and later (green) time points show CX3CR1(+) cell movement as green and red, while stable elements are yellow. Images are tracking the same animal over time. (b) A cell migration index (fraction of cells at the meningeal-electrode interface that are moving) shows that there is significantly greater migration at 0.5–0.75 dpi compared to 4–28dpi (one-way ANOVA, $p < 0.00001$; * denotes significant differences from both 0.5–1dpigroups with Tukey's HSD post-hoc tests, ^ denotes significance relative to 0.75–1 dpi only ; $p < 0.05$).Data presented as mean ± SEM, where n = 4 from 0.5–1dpi and 14–21dpi, n = 5 from 2–7dpi, and n =3 at 28dpi). (c) Migrating cells at 0.5–1dpi have a velocity of 3.04 ± 2.31 µm/min and a diameter of 10.31 ± 3.46 µm with no apparent relationship between these parameters (mean ± st. dev.) with a linear regression R-squared value of 0.02. Individual cells displayed in graph (n = 30). (d) Migrating cells show no clear preference (For each cell: net movement / total distance traveled) for migrating toward (blue bars) or away from (red bars) the interface.

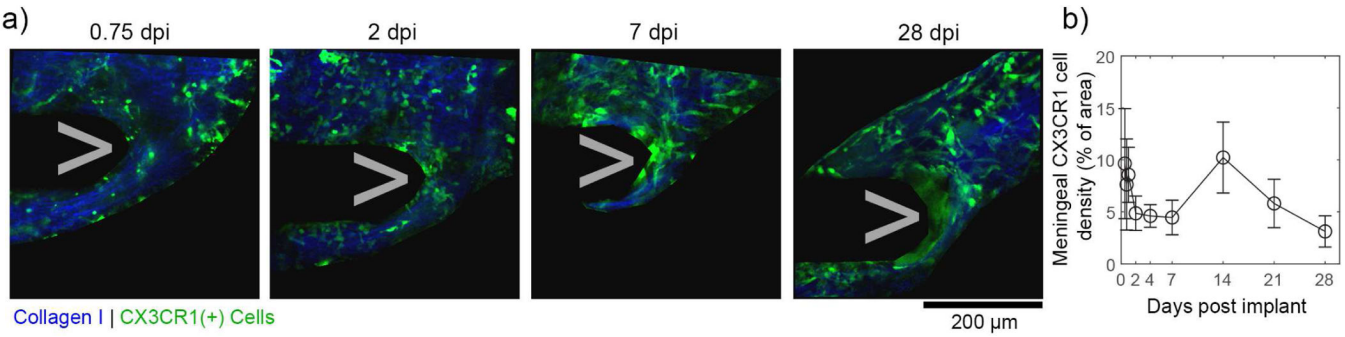

Figure 3.

Meningeal CX3CR1(+) cell densities fluctuate but are stable over the first month post implant. (a) Meningeal CX3CR1(+) cells (green) are automatically segmented from 3D image stacks if they are within or above the meninges (defined by continuous collagen I sheet; blue). These representative images track the same animal over the first month post implant. (b) The density of meningeal CX3CR1(+) cells (% of meningeal ROI that contains CX3CR1 signal) shows large fluctuations over time for each animal. Data presented as mean ± SEM, where n = 4 from 0.5–1dpi and 14–21dpi, n = 5 from 2–7dpi, and n =3 at 28dpi (not significant; one-way ANOVA $p = 0.5921$; n = 4).

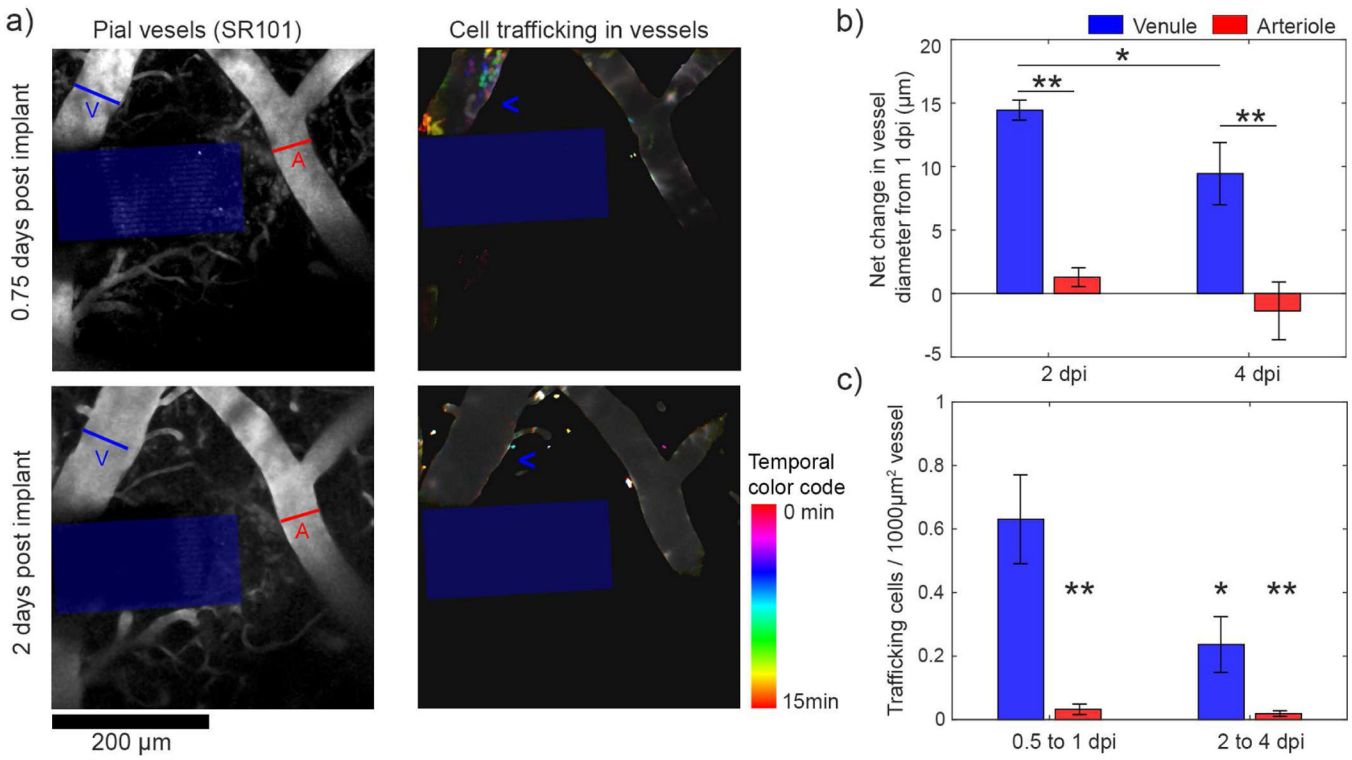

Figure 4.

CX3CR1(+) cell trafficking through pial venules during the first 4 dpi. (a) Left: Representative images of pial vessels labeled by SR101 at 18h (top) and 48h (bottom) post-implant adjacent to the electrode (blue box). An arteriole (red "A") and a venule (blue "V") were identified based on dilation response after implantation. Right: CX3CR1(+) cells within vessels were quantified over time. Frames over 15 minutes of imaging were superimposed, with each frame displaying a unique color defined by the "Time color code". Cells that migrate during a single frame retain the color of that frame, whereas cells that are stable over the imaging period appear as white. A region of high cell migration is seen in the venule (blue "<") at 18h, but not at 48h. (b) Large pial vessel diameters (12 vessels from 6 animals) were measured over time. Vessels that showed >10µm dilations were considered venules (blue). The net increase in venule diameter relative to 1 dpi was significantly greater than arterioles at 2 and 4 dpi (two-way ANOVA, $p < 0.01$ for group and time effects; significant differences with Tukey's HSD post-hoc test: ** = $p < 0.01$, * = $p < 0.05$). (c) Particle analysis of flowing cells detected significantly more cells migrating through venules at 0.5 to 1 dpi compared to arterioles at the same time as well as venules and arterioles at 2 to 4 dpi (two-way ANOVA, $p < 0.001$ for group effects; * ($p < 0.05$) and ** ($p < 0.01$) denotes significant decrease from venules at 0.5 to 1 dpi with Tukey's HSD post-hoc test). Data presented as mean ± SEM.

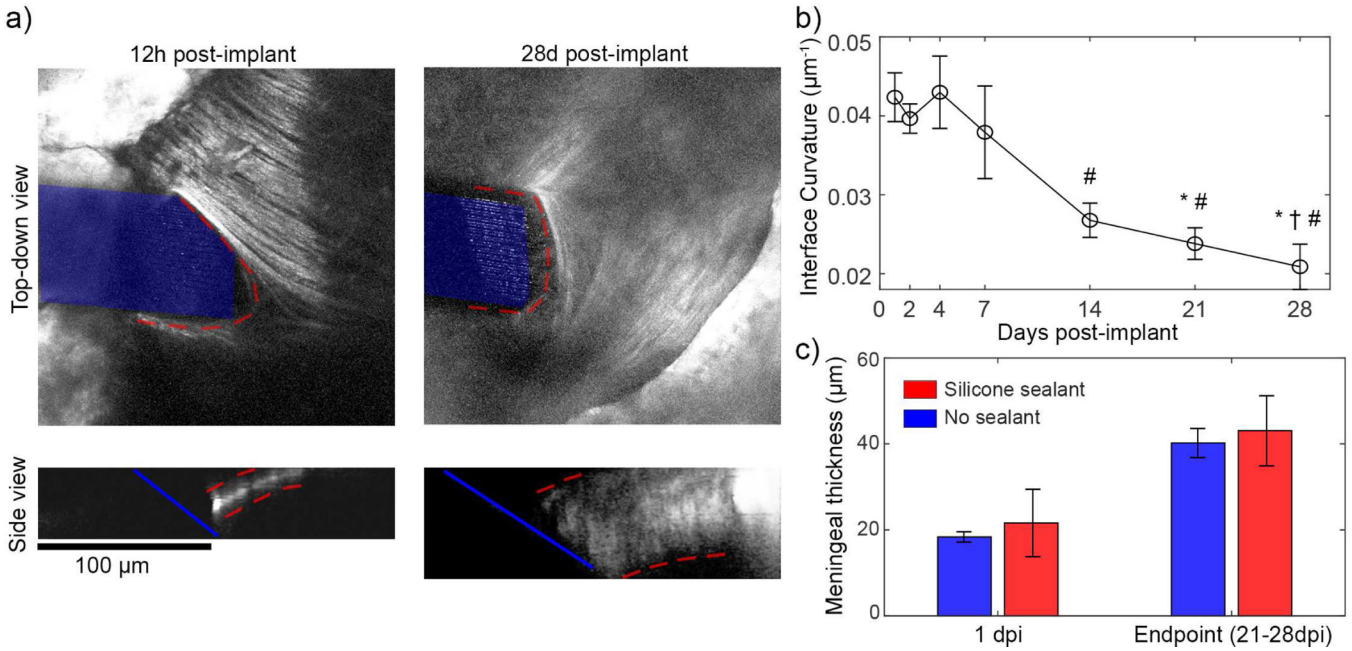

Figure 5.

Meningeal remodeling over the first month post implant. (a) Top-down views (top) of meningeal collagen I from the same animal at 12h and 28 days post implant reveals that, collagen-I (outlined in red) remodels to conform to the electrode surface (highlighted in blue). Side views (bottom) show that the meninges thicken (meninges outlined in red) (b) The curvature of collagen-I at the meningeal-electrode interface reduces over the first month, indicating a flatter, more conformal collagen interface (one-way ANOVA $p < 0.001$; significant reducMons relaMve to 1 dpi (*), 2 dpi (†), and 4 dpi (#) assessed with Tukey's HSD post hoc tests; $p < 0.05$). This analysis used all silicone sealed animals with visible meningeal-electrode interfaces (n = 4 for 0.5–21dpi, n = 3 for 28dpi) (c) Automated quantification of meningeal thickness within 1 dpi and at the experimental endpoint (between 21–28 dpi) shows statistically significant change in meningeal thickness over time (two-way ANOVA $p < 0.005$ for time effect; n = 6 for silicone at 1dpi, n = 5 for all other groups)). Sealant condition did not affect meningeal thickness, suggesting that the thickening was not in response to the presence of silicone. All data presented as mean ± SEM.

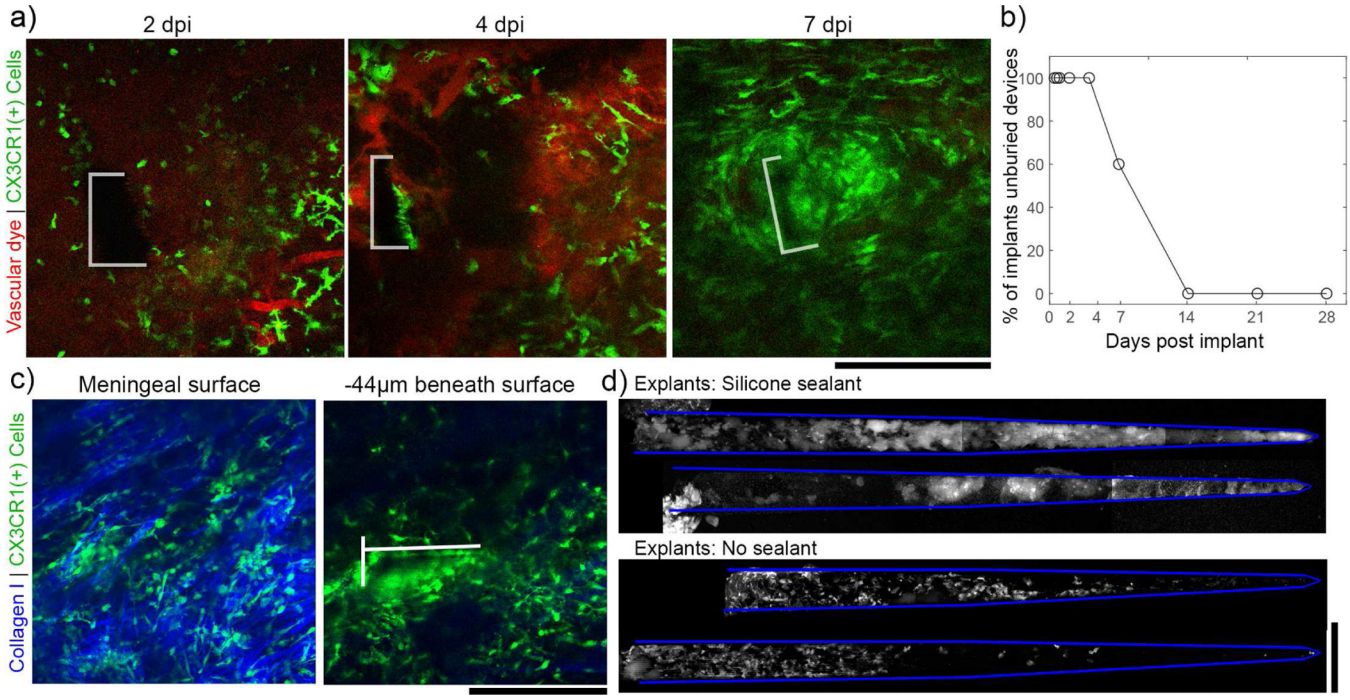

Figure 6.

Without the silicone sealant to fix the devices in place, electrodes were buried under the meninges by 14 dpi. (a) Representative images tracking the meningeal-electrode interface from the same animal over the first week post-implant (the electrode boundary is outlined in white). By 7 days post implant, the device is almost entirely buried in tissue. (b) For 5 devices implanted in craniotomies without silicone, 100% were completely buried in in tissue by 14 days post-implant. (c) Representative images from 21 dpi to confirm that, after being buried, electrodes are fully underneath meningeal collagen (left panel) and within the underlying cortex (right panel; the electrode is outlined in white). (d) CX3CR1(+) cells adhered to devices explanted at 28dpi from the silicone group (top) are morphologically distinct from those adhered to saline sealed devices (bottom). 2 explants are shown for each condition. All scale bars are 200 μm.

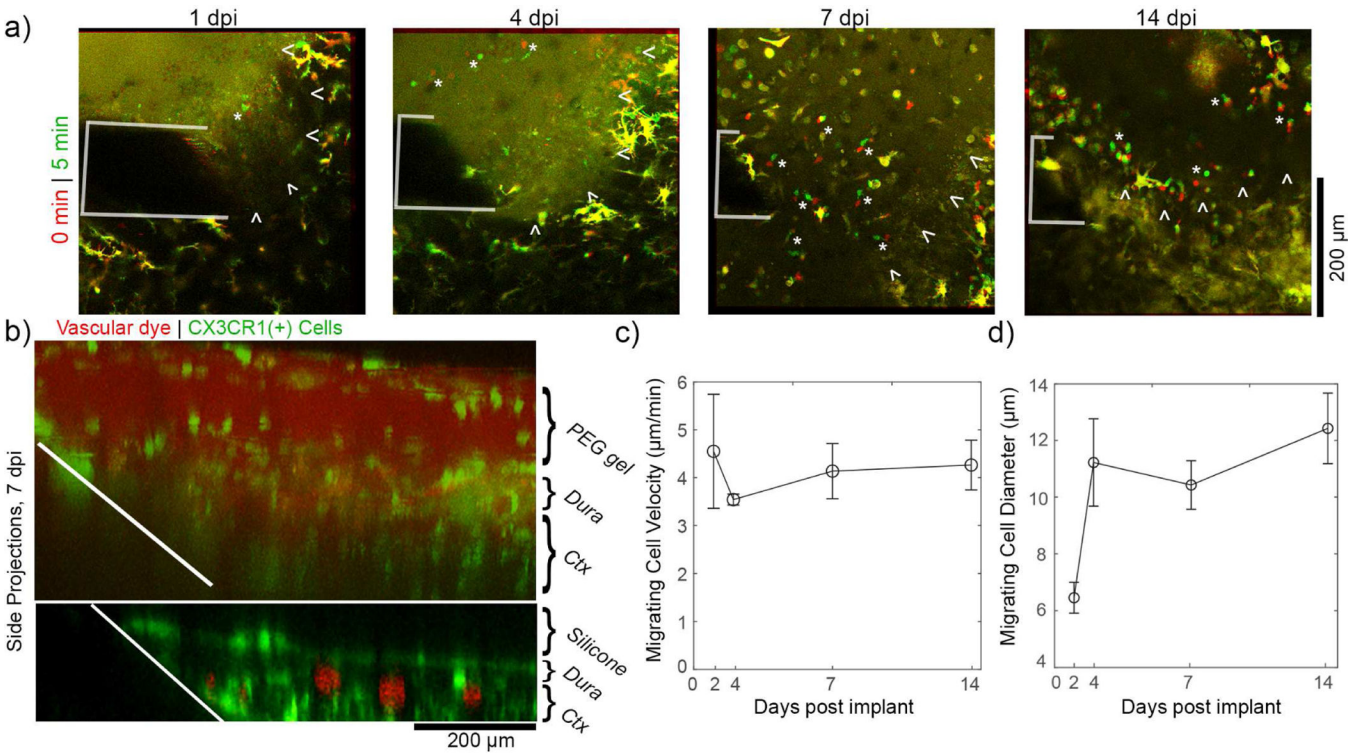

Figure 7.

In situ forming PEG/PEI hydrogels elicit a unique meningeal inflammatory response. (a) Meningeal CX3CR1(+) cells show robust migration through the PEG/PEI gel for at least 1 to 14 days post implant. Superimposed images at earlier time points (red) and later timepoints (green) show migrating cells as distinct red and green elements (denoted by white "*"), while stable elements are in yellow. The electrode is outlined in white. The boundary between the meninges and the hydrogel is denoted by white arrowheads. (b) Side projections at 7 dpi confirm that meningeal CX3CR1(+) cells (green) vascular dye (red) infiltrate the hydrogel (top) but not the silicone (bottom). (c) The velocity of cells migrating within the PEG/PEI gel are stable over 14 days. (d) The diameter of cells migrating within the PEG/PEI may increase after implantation (3–5 cells per time point, data presented as mean ± SEM).

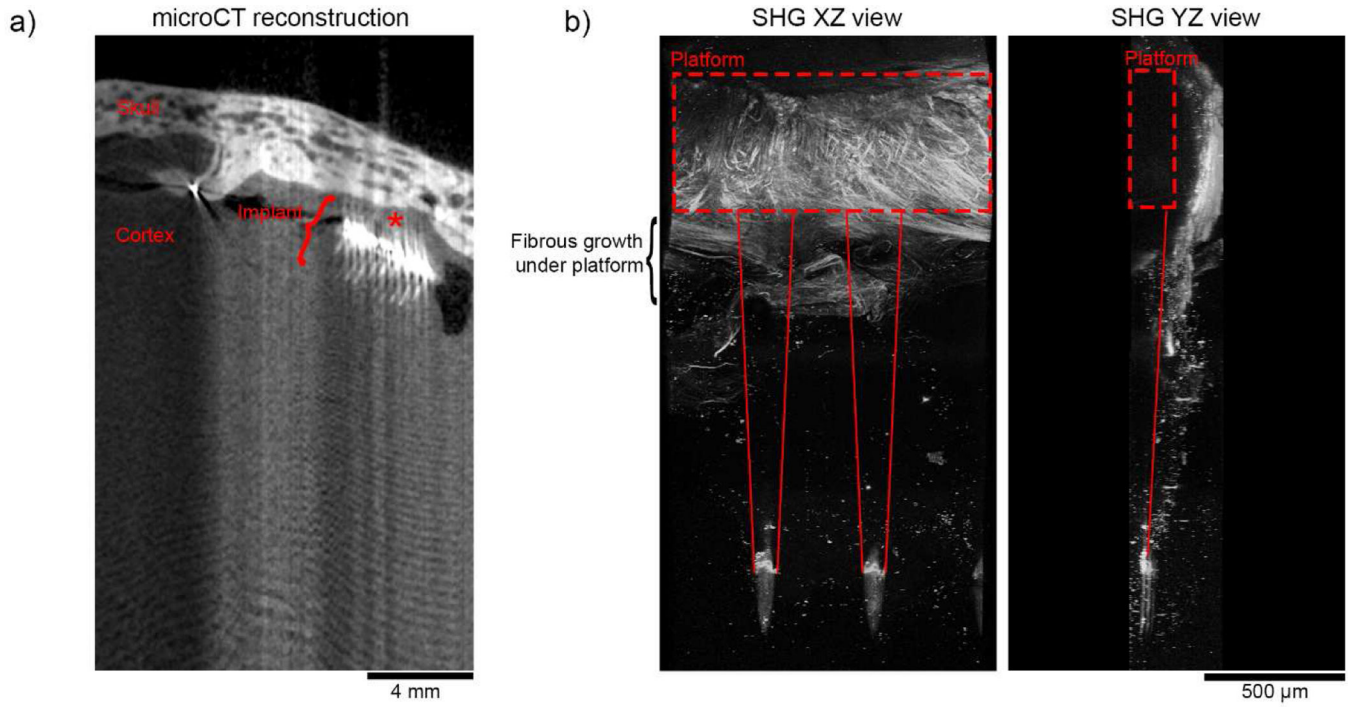

Figure 8.

Ex vivo imaging of fibrous encapsulation of Utah array platform implanted in a rhesus macaque for 2.5 years. (a) MicroCT reconstruction of the cortex and skull surrounding the implanted Utah array suggests that the array is still within the brain. Notably, soft tissues such as brain parenchyma and collagen I do not have sufficient contrast to be segmented in these images. Thick meningeal tissue is found above the device (red "*"). Optical aberrations are due to a metal artifact caused by the gold wiring at the array's platform. (b) Second harmonic imaging along the length of shanks shows significant fibrous collagen growth around the platform of the device (red dotted box). Importantly, The XZ plane image (left) shows that the fibrous growth extends beyond the platform to the shanks (outlined by solid red lines). A YZ side view (right) shows that that the meningeal collagen I has remodeled to curve around the device's platform. The signal at the tip of the devices is not morphologically consistent with collagen-I, and is likely an edge effect the parylene-C insulation.